PAPER

View Article Online
View Journal | View Issue

Ruthenium(II)-bisdemethoxycurcumin conjugate complexes as potent antitumour agents through simultaneous inhibition of 20S proteasome and HMG-CoA reductase†

Sara Pagliaricci,[a] Noemi Pagliaricci,[a] Alessia Tombesi, [ID] [a] Claudio Pettinari, [ID] [a] Massimiliano Cuccioloni,[c] Helena Juricic,[c] Agustín Galindo, [ID] [d] Farzaneh Fadaei-Tirani, [ID] [e] Riccardo Pettinari [ID] *[a] and Fabio Marchetti [ID] *[b]

The synthesis of new conjugated bisdemethoxycurcumin ligands, each incorporating a distinct acyl substituent—cyclic, aliphatic, heteroaromatic, or branched—in place of the native hydroxyl groups, has been reported. These ligands were employed to prepare the corresponding Ru(II)-*p*-cymene complexes, which were comprehensively characterized by FT-IR, NMR spectroscopy, elemental analysis, and ESI-MS. Single-crystal X-ray diffraction was used to elucidate the solid-state structures of two ligands and two metal complexes. Density Functional Theory (DFT) calculations provided further insights into the structural and electronic features of both the free ligands and their complexes. The anticancer potential of the Ru(II)-cymene compounds was assessed *in vitro* against a panel of human cancer cell lines (HepG2, Caco-2, and MCF-7), as well as non-tumorigenic controls. The complexes exhibited selective, cell-type-specific cytotoxicity, primarily mediated through proteotoxic stress—evidenced by proteasome inhibition and p62 accumulation—and HMG-CoA reductase-dependent downregulation of PCNA expression.

Introduction

The unique characteristics of transition metals—such as their wide range of oxidation states and coordination geometries—enable a diverse array of structural possibilities and mechanisms of action for metal-based drugs, which are often not achievable with purely organic molecules.[1] Currently, platinum-based compounds play a pivotal role in cancer treatment regimens. These drugs primarily exert their effect by binding to DNA, forming cross-links that inhibit replication and transcription. This disruption induces cellular dysfunction and ulti-

mately triggers apoptosis.[2] Ruthenium complexes have emerged as promising candidates in the development of anti-cancer agents due to their distinctive chemical properties and favourable biological profiles. Notably, they can overcome known mechanisms of platinum resistance and act through alternative pathways, including mitochondrial-mediated apoptosis and death receptor signalling.[3–5] Among these, two classes of ruthenium(II)–arene complexes—RAED and RAPTA—have gained particular interest for their anticancer and antimetastatic properties. Turmeric (*Curcuma longa*) is a well-known source of curcuminoids, a class of phytochemicals with a long-standing history in traditional medicine for treating a variety of conditions, including skin diseases, respiratory disorders, gastrointestinal issues, wounds, and liver dysfunction.[6,7] Although turmeric contains approximately 235 bioactive compounds, its therapeutic effects have been primarily attributed to curcumin. Curcumin (CurcH), which is chemically described as 1,7-bis-(4-hydroxy-3-methoxyphenyl)-hepta-1,6-diene-3,5-dione, is a lipophilic polyphenol belonging to the curcuminoid family.[8,9]

However, its poor chemical stability and rapid metabolic degradation result in low bioavailability, representing a major limitation to its clinical application.[10] These issues are also observed in the two other main curcuminoids—demethoxycurcumin (DCurcH) and bisdemethoxycurcumin (BDCurcH)—which differ from CurcH by the absence of one or

[a]*School of Pharmacy, University of Camerino, via Madonna delle Carceri, 62032 Camerino, MC, Italy*

[b]*School of Science and Technology, University of Camerino, via Madonna delle Carceri, 62032 Camerino, MC, Italy*

[c]*School of Biosciences and Veterinary Medicine, University of Camerino, via Madonna delle Carceri, 62032 Camerino, MC, Italy*

[d]*Departamento de Química Inorgánica, Facultad de Química, Universidad de Sevilla, Aptdo 1203, 41071 Sevilla, Spain*

[e]*Institut des Sciences et Ingénierie Chimiques, École Polytechnique Fédérale de Lausanne (EPFL), 1015 Lausanne, Switzerland*

two methoxy groups, respectively (Fig. 1).[11] Among them, BDCurcH shows improved chemical stability and reduced susceptibility to degradation under physiological conditions. Importantly, while CurcH exhibits general anti-inflammatory properties, BDCurcH has demonstrated specific inhibitory activity against key inflammatory pathways, particularly the NF-κB signalling cascade, which plays a central role in regulating inflammation.[12] CurcH has been widely studied for its anticancer, neuroprotective, and anti-angiogenic potential.[13] In contrast, BDCurcH has received comparatively limited attention regarding its anticancer activity.[14,15] Our research group has systematically studied Ru(II) half-sandwich complexes with various curcuminoids to explore structure–activity relationships (SARs).[18] Despite most previous work focused on curcumin,[16,17] our results show that complexes containing bisdemethoxycurcumin consistently display higher cytotoxicity and selectivity than those with curcumin, regardless of the other substituents present on the metal centre.[19] Identifying bisdemethoxycurcumin as the key bioactive component, despite its lower natural abundance in turmeric, offers a strong rationale for structure-guided design and highlights its potential as a privileged scaffold for developing new metal-based therapeutics. Consequently, recent efforts have concentrated on synthesizing and characterizing the most promising bisdemethoxycurcumin-based Ru(II) complexes. In this study, we report the synthesis and characterisation of novel BDcurcH-based ligands and investigate the influence of varying ester residues on their biological activity. These ligands were subsequently used to form corresponding ruthenium(II)–arene complexes, which were examined to determine whether metal coordination enhances their solubility, chemical stability, and antitumour efficacy (Fig. 2).
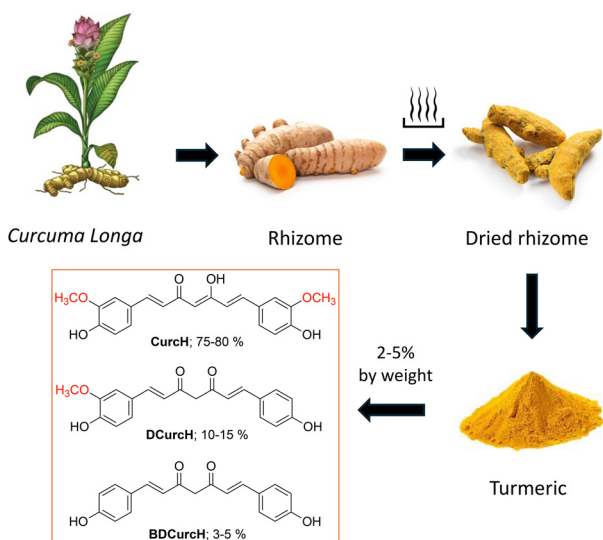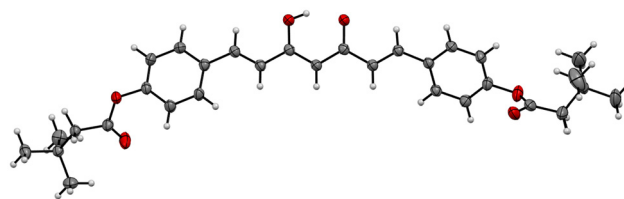

Fig. 2 Molecular structure of compound **HL**[4]. Color codes: C, grey; H, white; O, red.

Results and discussion

The ligands **HL**[1]–**HL**[4] were synthesised *via* nucleophilic substitution reactions between the phenolic groups of BDcurcH and various acyl chlorides bearing cyclic, aliphatic, heteroaromatic, or branched moieties. The synthetic procedure involved dissolving BDcurcH in acetone, followed by the addition of triethylamine (TEA) to generate a basic medium conducive to deprotonation of the two phenolic –OH groups. The esterification reaction was then initiated by the dropwise addition of an excess of the appropriate acyl chloride at 0 °C: cyclopentanecarbonyl chloride for **HL**[1], heptanoyl chloride for **HL**[2], 2-furoyl chloride for **HL**[3], and 3,3-dimethylbutyryl chloride for **HL**[4] (Scheme 1). In the IR spectra of the **HL**[1]–**HL**[4] ligands, the disappearance of the broad absorption band above 3000 cm^{-1}, corresponding to the O–H stretching vibrations of the phenolic groups in the starting material BDcurcH, was observed. Furthermore, all characteristic absorption bands of the newly formed ester functionalities, particularly those associated with the –OC=O stretching vibrations, were present in the final spectra. The structures of **HL**[1]–**HL**[4] were confirmed by mass spectrometry, as well as by ^{1}H, ^{13}C NMR, and two-dimensional NMR spectroscopy (see ESI†). Additionally, suitable single crystals of **HL**[2] and **HL**[4] were obtained, and their X-ray crystallographic analysis confirmed the successful formation of the targeted BDcurcH-conjugates Complexes **1**–**4** were synthesised in good yields by dissolution of the corresponding curcuminoid-conjugates in acetonitrile in the presence of one equivalent of triethylamine, which acts to deprotonate the ligands. After 30 minutes of stirring, the dimer $[(p\text{-cym})RuCl_2]_2$ (p-cym = *para*-cymene) was added, and the resulting red solution was refluxed for 16 hours (Scheme 2).

Complexes **1**, **2** and **4** are readily soluble in acetonitrile. Their solutions were concentrated using a rotavapor, and the residues were recrystallised with a CH_2Cl_2/hexane mixture. In contrast, complex **3**, which is only sparingly soluble in acetonitrile, was isolated by filtration and subsequently recrystallized using the same solvent system. Compounds **1**–**4** are airstable and display good solubility in acetone, chlorinated solvents, and DMSO, while exhibiting only limited solubility in methanol, ethanol, diethyl ether, and petroleum ether. The IR spectra of **1**–**4** exhibit the characteristic ν(C=O) vibrations at lower wavenumbers than in the corresponding free ligands, which can be attributed to coordination through both oxygen atoms to the metal. In the far-IR region, strong absorptions in

Fig. 1 From *Curcuma longa* to curcuminoids.
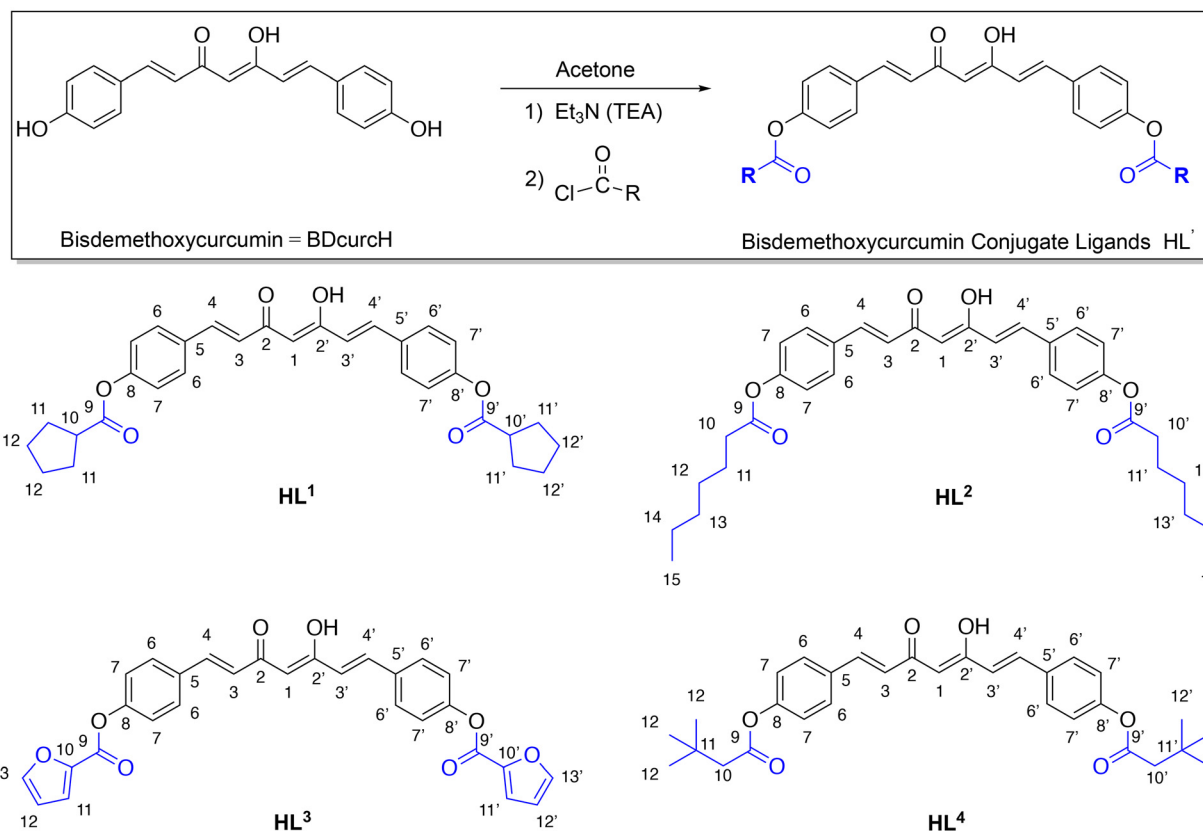
Scheme 1 Synthesis of ligands HL^1–HL^4.
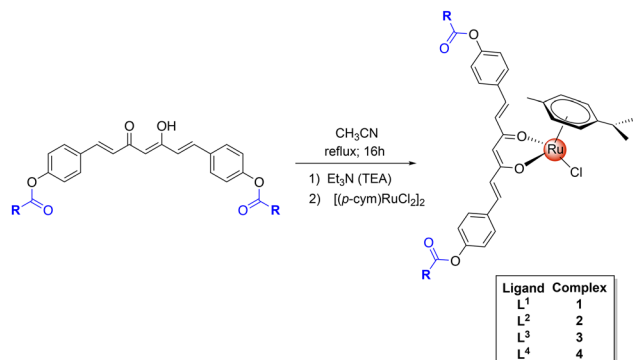
Scheme 2 Synthetic procedure for complexes **1–4**.

the range between 276 and 281 cm^{-1} may be assigned to ν(Ru–Cl) stretching. Electrospray ionization mass spectrometry (ESI-MS) was performed in positive-ion mode using acetonitrile solutions of the complexes. The spectra confirmed the molecular structures through the presence of molecular ion peaks corresponding to the general fragment $[(p\text{-cym})Ru(L')]^+$, which result from the loss of the chloride ligand. Conductivity measurements carried out over 72 hours revealed that all complexes remain predominantly neutral in solution. The conductivity values in DMSO ranging from 10 to 11 $\mu S\ cm^2\ mol^{-1}$ suggests only a weak ionization process at 298 K due to the

partial chloride dissociation and formation of solvated $[(p\text{-cym})Ru(L')]^+$.

X-ray structural characterization

The precursor ligands HL^2 and HL^4 were analysed by single-crystal X-ray crystallography. They crystallised in monoclinic space groups $P2_1$ and $P2_1/n$, respectively. Both compounds are characterised by the presence of an intramolecular hydrogen bond between the hydrogen atom of the OH group and the oxygen atom of the C=O group (O···O distance of 2.457(3) Å for HL^4). The discussion of selected structural parameters will focus on HL^4 (Fig. 2) because HL^2 (Fig. S34†) has a slightly high R-factor (10.7%). The olefinic C=C bond distances for HL^4 are both 1.392(1) Å, while the C=O and C–OH bonds lengths of the keto–enol group are 1.284(2) and 1.315(1) Å, respectively. The angles within the keto–enol moiety are all close to the expected value of 120°. Other structural parameters are typical and no requires further discussion (see Table S2†). The crystal packing in both compounds (Fig. S34 and S35†) is not dominated by potential π-stacking interactions of the phenyl rings.

Complexes **1** and **3** were recrystallised from dichloromethane/hexane and structurally characterised by single-crystal X-ray crystallography. The resulting molecular structures are shown in Fig. 3 and 4, respectively.
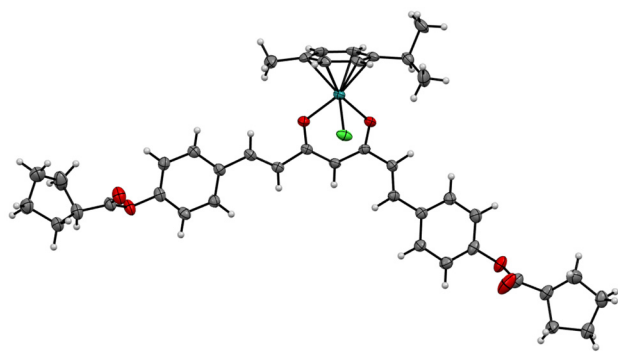
Fig. 3 Molecular structure of complex **1**. Color codes: C, grey; H, white; O, red; Cl, green; Ru, turquoise.
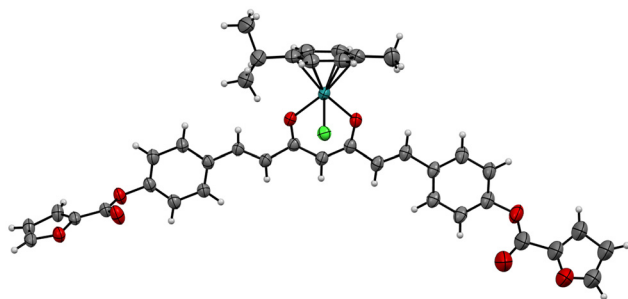

Fig. 4 Molecular structure of complex **3**. Color codes: C, grey; H, white; O, red; Cl, green; Ru, turquoise.

The typical piano stool geometry was observed for both complexes with normal Ru–Cl bond lengths of 2.4071(8) and 2.424 (2) Å for **1** and **3**, respectively. The Ru–O bond lengths, which range from 2.061(4) to 2.077(2) Å, are comparable to those found in related ruthenium-curcumin derivatives.[19] The ester substituent does not significantly influence the observed bond distances within the delocalized six-membered metallacycle or the olefinic bond of both structures, in comparison to related Ru–curcumin complexes (C⋯O close to 1.29 Å, C⋯C around 1.38–1.39 Å, and C=C equal to 1.33 Å).[20] In both structures, the ligands L^1 and L^3 are essentially planar, except for the ester moieties. Other structural parameters are collected in Table S4.† Two different conformations of the coordinated L^1 and L^3 ligands were observed around the (O)C–CH = bond. In **3**, the relative orientations of oxygen and hydrogen atoms around this bond are all *transoid* (O–C–C–H torsion angles of approximately 177°). By contrast, in complex **1**, one orientation is *transoid* and the second *cisoid* with an O–C–C–H torsion angle of 14.0°.

Theoretical studies

The precursor ligands HL^1–HL^4 and their L^1–L^4 anions were analysed using density functional theory (DFT) at the B3LYP/6-311G* theoretical level. The resulting optimised structures are shown in Fig. S36,† while selected bond lengths and angles are collected in Tables S2 and S3.† As expected, the C⋯O bond

lengths of the anions (*ca.* 1.242 Å) are intermediate between the C=O and C–OH distances calculated for the precursor ligands HL^1–HL^4. Similarly, the alternation of C=C and C–C bonds within the keto–enol moiety (around 1.379 and 1.443 Å, respectively), which is observed in compounds HL^1–HL^4, disappears in the anions, where delocalization is observed (C⋯C bond distances close to 1.425 Å). The olefinic C=C bond lengths of the anions (mean value 1.343 Å) remain essentially unchanged with respect to those of the parent precursor ligands (mean value 1.346 Å). The coordination capabilities of the L^1–L^4 ligands toward the ruthenium center in complexes **1–4** were analysed by inspecting the MOs of optimised anions. The ligands are characterised by a HOMO constituted by the π part of the metallacycle. The out-of-phase and in-phase combinations of *in-plane* oxygen orbitals are observed in HOMO−1 and HOMO−2, respectively. These MOs are involved in σ-coordination to the ruthenium center. The energies of these orbitals are very similar, which implies that the ester substituent does not significantly influence the donor capacities of these ligands (Fig. S37).†

The ruthenium complexes **1–4** were also investigated using DFT at the B3LYP/LANL2DZ/6-311G* theoretical level. Their optimised structures are shown in Fig. 5. The selected combination of method and basis sets provides a satisfactory structural description of these complexes, as deduced from the comparison of the structural parameters of **1** and **3** with those determined by X-ray diffraction (Table S4†). The calculated Ru–Cl and Ru–O bond lengths have mean values of 2.443 and 2.094 Å, respectively (Table S4†). This fits well with the Mayer bond orders calculated for these bonds in complexes **1–4** (Table S5†), which are quite similar for the four types of ester substituents. The delocalization within the metallacycle is revealed by the C⋯O and C⋯C bond lengths (mean values of 1.279 and 1.405 Å, respectively). The former is slightly longer, while the latter is slightly shorter than those calculated for the corresponding L^1–L^4 anions. The presence of different conformers in the ligands of complexes **1** and **3** prompted us to analyze the existence of rotamers around the (O)C–CH = bond. Three possible rotamers (*transoid-transoid*, *transoid-cisoid* and *cisoid-cisoid*) were optimised (Fig. S38†). The most stable rotamer for both complexes is the *transoid-transoid*. In the molecular structure of **1** the conformation detected is *transoid-cisoid*, which is destabilised by
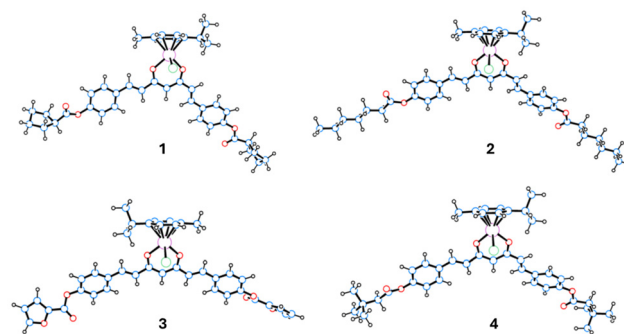

Fig. 5 Optimised structures of the complexes **1−4**.

only 4.9 kcal mol^{-1} (as relative $\Delta G_{\text{gas–phase}}$, see Table S6†). By contrast, the molecular structure of **3** shows the *transoid-transoid* conformation and the *transoid-cisoid* rotamer has almost the same energy (energy difference: less than 1 kcal mol^{-1}). The most destabilised conformer for both complexes is the *cisoid-cisoid*, which has not been experimentally observed, being higher in energy by 4.9 and 3.6 kcal mol^{-1} for **1** and **3**, respectively (Table S6†). Additionally, we selected ligand L^3 and optimised their three possible rotamers corresponding to the *transoid–transoid*, *transoid–cisoid* and *cisoid–cisoid* conformers (Fig. S6†). Again, the most stable was the *transoid–transoid* rotamer, observed in the X-ray structure of **3**. The *transoid–cisoid* conformation, which was present in **1**, is destabilised by 4.8 kcal mol^{-1} (as relative $\Delta G_{\text{gas–phase}}$), while the most destabilised is the *cisoid–cisoid* conformer (less stable by 8.4 kcal mol^{-1}, see Table S6†). The coordination of L^1–L^4 to the Ru metal produces a reduction of the angles C⋯C⋯O and C⋯C⋯C of the metalla-cycle. This circumstance leads to energy differences between the conformers that are smaller in complex **3** than those calculated for the free ligand L^3.

Biological studies

UV-Visible stability studies

To investigate the stability profile under physiologically relevant conditions, phosphate-buffered solutions (PBS, pH = 7.4) of all the complexes were monitored over time using UV-Visible spectroscopy. The complexes were initially dissolved in DMSO (about 0.7 mg L^{-1}) and then diluted to 5% the DMSO with PBS. The absorbance spectra were collected after 0, 24, 48 and 72 h (Fig. S40†). From the spectra is possible to deduce that, generally, the complexes suffer an abrupt decrease in the absorbance after the first 24 hours and, after that, they result unchanged during time. The complex **3** containing the more polar hetero-cyclic 2-furoyl group is the most stable while the less stable specie is **2** which contain the long aliphatic chains which result more hydrophobic. Moreover, the BDCurcH-conjugated with acyl chlorides possessing a cyclic structure generally show a more stable trend in decreasing absorbance. A possible explanation for the decrease of absorption energy over time by the complexes may be attributed to precipitation phenomena, observable by clouding of the solution, probably due to the very high lipophilic character of curcuminoids residue. The ^{1}H NMR spectra of the insoluble fraction formed after 24 hours in the physiological solution (H$_2$O–DMSO–PBS) confirm that, in all cases, the precipitates correspond to the initial ruthenium complexes (see Fig. S41–S43†). However, no changes were observed in the absorption wavelength, this means that the coordination environment result unchanged. All the complexes showed transitions in the range 350–400 nm assignable to MLCT (metal–ligand charge transfer) from the filled 4d orbitals of Ru(II) to the empty π* ligand orbitals (4d^6 Ru → π*).

Cytotoxicity

The cytotoxicity of free ligands and their corresponding Ru-complexes was evaluated against human hepatocarcinoma (HepG2), colorectal adenocarcinoma (Caco-2), breast cancer (MCF-7) cell lines, and non-tumorigenic MCF10A cells. The resulting IC$_{50}$ values of the compounds are presented in Table 1 together with the values for cisplatin used as a control. The formation of ruthenium complexes resulted in a significant enhancement of the cytotoxic potential of HL^1–HL^4 free ligands. Complexes **1–4** exhibited variable cytotoxic rankings across the cancer cell lines tested, generally achieving cisplatin-like IC$_{50}$ values in the low micromolar range. Notably, all Ru(II)-complexes exhibited enhanced potency compared to cisplatin against Caco-2 cells. Excluding complex 3, all complexes exhibited promising selectivity for MCF7 breast cancer cells, with up to 5-fold higher cytotoxicity than non-tumorigenic MCF10A.

DNA binding

The DNA binding ability of HL^1–HL^4 free ligands and their and **1–4** complexes was evaluated using a Surface plasmon resonance (SPR) biosensor. The mono-exponential nature of binding kinetics for all the compounds is consistent with the presence of a single high-affinity site on DNA (Fig. 6 and Fig. S44†). Ligands and metal complexes demonstrated fully reversible binding behaviour, with equilibrium dissociation constants in the range 1–29 μM, reflecting moderate affinity interactions regulated by binding thermodynamics (Table 2).

Effect on proteasome activity

Proteasome inhibition by the HL^1–HL^4 free ligands and complexes **1–4** was evaluated with respect to three major activities of 20S proteasome, namely chymotrypsin-like (ChT-L), trypsin-like (T-L) and caspase-like activities (Casp-L) (Table 3). The free ligands did not inhibit proteasome hydrolytic activities in the range of concentrations tested. In contrast, complexes **1–4** inhibit proteasome hydrolytic activities, with a pronounced effect against ChT-L activity and a less significant effect on T-L activity. It is important to note that no enhancement of Casp-L

Table 1 Cytotoxicity of HL^1–HL^4 and **1–4** towards HepG2, MCF7, Caco-2 cancer cell lines, as well as non-tumorigenic MCF10A cells. IC$_{50}$ values (in μM) represent the mean from three independent experiments $\pm$ standard deviation following exposure to the compounds for 72 h

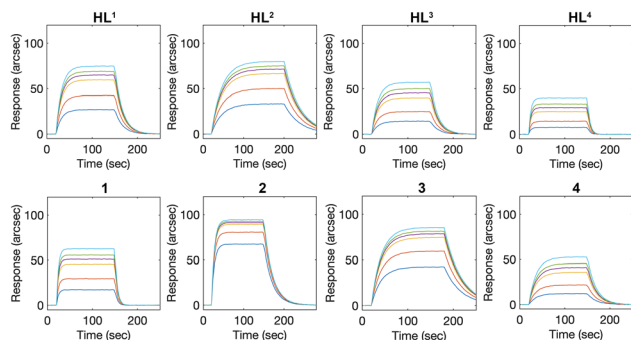| Compound	HepG2	CaCo-2	MCF7	MCF10A	Selectivity index
HL^1	>100	>100	>100	>100	—
HL^2	>100	>100	>100	>100	—
HL^3	>100	>100	>100	>100	—
HL^4	>100	>100	>100	>100	—
1	3 ± 0.5	5 ± 1.8	4 ± 0.4	22 ± 1.7	5.5
2	8 ± 2.1	5 ± 1.4	13 ± 0.5	41 ± 0.6	3.2
3	6 ± 2.0	13 ± 1.8	12 ± 1.9	10 ± 0.6	0.8
4	4 ± 1.3	5.5 ± 0.9	2.5 ± 0.8	9 ± 0.2	3.6
Cisplatin	1.4 ± 0.7	18 ± 1.9	4.2 ± 2.3	1.2 ± 0.2	0.3

Fig. 6 Representative superimposition of sensorgrams obtained upon binding of soluble **HL¹**–**HL⁴** free ligands and complexes **1**–**4** to a surface-anchored dsDNA oligomer.

Table 2 Kinetic and equilibrium parameters for the interaction between **HL¹**–**HL⁴**, complexes **1**–**4**, and surface-blocked DNA oligomer

Compound	k_{ass} (M⁻¹ s⁻¹)	k_{diss} (s⁻¹)	K_D (µM)
HL¹	8910 ± 1633	0.06 ± 0.02	6.78 ± 2.00
HL²	5215 ± 667	0.03 ± 0.01	5.01 ± 2.01
HL³	4156 ± 692	0.06 ± 0.01	15.04 ± 3.15
HL⁴	6310 ± 625	0.19 ± 0.05	29.91 ± 8.06
1	16 676 ± 2541	0.19 ± 0.02	11.99 ± 2.16
2	3933 ± 359	0.05 ± 0.04	1.21 ± 0.92
3	8049 ± 822	0.03 ± 0.01	3.40 ± 1.40
4	2979 ± 380	0.05 ± 0.01	18.02 ± 2.63
Cisplatin	23 657 ± 1508	0.004 ± 0.001	0.10 ± 0.02

Table 3 IC₅₀ values for **HL¹**–**HL⁴** and **1**–**4** against proteasomal activity

Compound	ChT-L (µM)	T-L (µM)	Casp-L (µM)
HL¹	>100	>100	>100
HL²	>100	>100	>100
HL³	>100	>100	>100
HL⁴	>100	>100	>100
1	12.55 ± 0.31	>100	>100
2	13.91 ± 0.96	>100	>100
3	13.91 ± 0.57	19.88 ± 1.5	>100
4	12.17 ± 0.85	86.03 ± 1.1	>100
Bortezomib	$(1.0 ± 0.2)^{-3}$	>100	0.10 ± 0.03

inhibition was observed. The positive correlation between cytotoxicity and 20S proteasome inhibition suggested that the 20S proteasome is likely a relevant target for these complexes. In particular, the dominant ChT-L inhibition indicated its primary role in the observed anticancer effects, whereas the modest T-L inhibition may offer a supporting mechanism.

HMG-CoA reductase binding/inhibition

HMG-CoA reductase, a key enzyme in cholesterol synthesis, is an emerging anticancer target. Its inhibition disrupts cell signalling and membrane integrity, impacting cancer cell growth
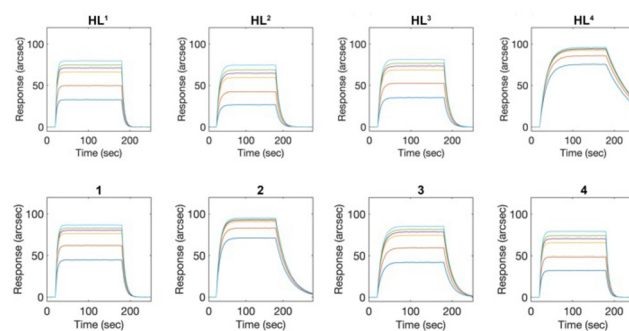

Fig. 7 Representative superimposition of sensorgrams obtained upon binding of soluble **HL¹**–**HL⁴** ligands and complexes **1**–**4** to a surface-anchored HMGR.

and survival pathways. Both proligands and ruthenium complexes were shown to bind to HMGR and inhibit its activity with moderate affinity/potency, with a general ameliorative effect induced by metal incorporation (Fig. 7 and Table 4), in line with previous evidence on the effect of Ru-complexation of small ligands toward HMGR.[21,22] Similar to the effect observed on proteasome, the enhanced HMGR inhibition positively correlated with the observed cytotoxicity against cancer cells.

According to the results above reported, complex **1** showed the best toxicity profile and cell selectivity. Further investigations on cell permeability and impact on some relevant biomarkers, including proliferating cell nuclear antigen (PCNA) and the multifunctional protein p62, were carried out on **1** and the respective free ligand **HL¹**.

Cell permeability

The transmembrane transport of complex **1** and its proligand **HL¹** was evaluated by monitoring the changes in membrane fluidity in Caco-2 cells using the fluorescent probe trimethylammonium diphenylhexatriene (TMA-DPH). No significant alterations in membrane fluidity were observed that could be correlated with their cytotoxicity profiles (Fig. 8).

Both compounds exhibited single perturbation events in membrane fluidity, the event peaking at 80 min **HL¹**, while the larger complex **1** displayed a delayed peak at 110 min. This kinetic lag aligns with size-dependent internalization rates. A minor secondary signal at 80 min for **1** suggested the partial

Table 4 Kinetic, equilibrium and inhibitory parameters of **HL¹**–**HL⁴** and **1**–**4** binding to HMGR

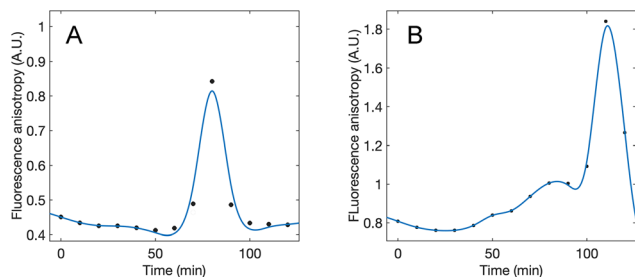| Compound	k_{ass} (M⁻¹ s⁻¹)	k_{diss} (s⁻¹)	K_D (µM)	K_i (µM)
HL¹	39 025 ± 1741	0.19 ± 0.07	4.87 ± 1.81	6.30 ± 2.81
HL²	14 667 ± 853	0.10 ± 0.01	6.82 ± 0.79	8.11 ± 2.36
HL³	21 003 ± 1061	0.09 ± 0.01	4.29 ± 0.52	5.22 ± 1.34
HL⁴	18 943 ± 1484	0.10 ± 0.02	5.28 ± 1.13	6.00 ± 0.88
1	46 922 ± 8903	0.08 ± 0.03	1.70 ± 0.72	1.30 ± 0.55
2	29 844 ± 3687	0.03 ± 0.01	1.01 ± 0.36	1.28 ± 0.48
3	16 109 ± 2616	0.05 ± 0.01	3.10 ± 0.80	3.48 ± 1.16
4	29 769 ± 2303	0.06 ± 0.02	2.02 ± 0.69	3.04 ± 0.86
Simvastatin	—	—	—	2.0 ± 0.3

Fig. 8 Comparative changes in emission anisotropy with time observed upon internalization of parent ligand HL[1] (Panel A) and 1 (Panel B).

degradation of the complex during membrane transit. The observed kinetics were collectively consistent with an endocytosis-driven internalization pathway, which involves transient membrane restructuring during vesicle formation.

Effects on cellular biomarkers

To assess the impact of 20S proteasome and HMG-CoA reductase inhibition, and to identify the possible mechanism of cell death induced by the molecules of interest, we monitored the expression levels of p62 (a multifunctional adaptor protein involved in autophagy and cellular stress responses)[23] and PCNA (an established marker of cell proliferation that reflects the cellular response to cholesterol synthesis disruption)[24] in Caco-2 cells treated with complex 1 and HL[1] (Fig. 9).

In line with their effects on Caco-2 cells viability, the exposure to complex 1 resulted in a marked 25% increase in p62 levels compared to the control ($p < 0.05$), indicating a possible block in autophagic flux,[25] whereas the curcuminoid ligand alone did not significantly alter p62 expression, exhibiting levels comparable to the control. Conversely, both complex 1 and HL[1] induced a comparable 25% decrease in PCNA expression ($p < 0.05$), this downregulation being consistent
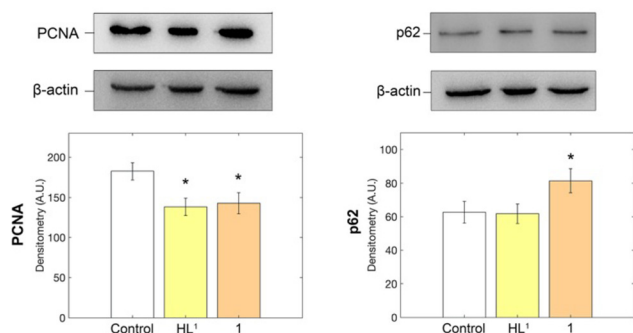

Fig. 9 Changes in cellular PCNA and p62 levels in Caco-2 cells treated with either 2 μM of HL[1] or complex 1 for 24 h (left and right panel, respectively). Results are representative of three distinct experiments. Data points marked with an asterisk are significantly different compared to internal controls (*$p < 0.05$). Equal protein loading was verified using β-actin.

with the arrest cell cycle and reduced tumour growth potential,[26] but likely to have a secondary role on Caco-2 cell viability.

Conclusions

In this work, we obtained four esterified derivatives of bisdemethoxycurcumin, each featuring a different acyl group-cyclic, aliphatic, heteroaromatic, or branched. These pro-ligands were subsequently used to prepare a series of ruthenium(II)-p-cymene complexes. Both the free ligands and their corresponding metal complexes were comprehensively characterized in solution and in the solid state. The ruthenium complexes significantly enhanced the cytotoxicity of the curcuminoid ligands across various cancer cell lines. Consistent with our data on cell membrane permeability, suggesting an endocytosis-mediated uptake, the Ru–bisdemethoxycurcuminoid complexes elicited significant cytotoxic effects upon internalization, particularly against Caco-2 cells, where their efficacy and selectivity surpassed those of cisplatin. Mechanistically, their anticancer activity appears to arise from a multitargeted mode of action: primarily through proteotoxic stress *via* proteasome inhibition and p62 accumulation, and secondarily through HMG-CoA reductase–mediated downregulation of PCNA expression, ultimately leading to cancer cell death. The Ru(II)–curcuminoids complexes here investigated act through multiple targets by moderately inhibiting proteasome activity, HMG-CoA reductase, and binding reversibly to DNA. This combined action disrupts key functions in cancer cells, such as DNA replication, protein degradation, and cholesterol production, leading to enhanced cell death. Cancer cells (HepG2, MCF7, CaCo-2) are more vulnerable to these effects due to higher oxidative stress and metabolic problems, while normal cells (MCF10A) are less affected thanks to better detoxification and stress responses. These complexes selectively trigger apoptosis in cancer cells under stress, showing an advantage over drugs that act on a single target. Overall, their multitarget activity and good cytotoxic profile make them promising candidates for new metal-based anticancer drugs.

Experimental

Materials and methods

The dimer [(cymene)RuCl$_2$]$_2$ was purchased from Aldrich while curcumin and bisdemethoxycurcumin were purchased from TCI Europe and were used as received. All other materials were obtained from commercial sources and were used as received. IR spectra were recorded from 4000 to 200 cm^{-1} with a PerkinElmer Spectrum 100 FT-IR instrument. ^{1}H, ^{13}C NMR, {^{1}H–^{1}H}-COSY NMR, {^{1}H–^{13}C}-HSQC and {^{1}H–^{13}C}-HMBC spectra were recorded on a 500 Bruker Ascend (500.1 MHz for ^{1}H and 100 MHz for ^{13}C) and a 400 Mercury Plus Varian instrument (400 MHz for ^{1}H and 100 MHz for ^{13}C). Referencing is relative to TMS (1H). Coupling constants are given in Hz.

Positive and negative ion electrospray ionization mass spectra (ESI-MS) were obtained on a Series 1100 MSI detector HP spectrometer using methanol or acetonitrile as the mobile phase. Solutions for analysis (3 mg mL^{-1}) were prepared using reagent-grade methanol and acetonitrile. Masses and intensities were compared to those calculated using IsoPro Isotopic Abundance Simulator, version 2.1.28. Melting points were recorded on an STMP3 Stuart scientific instrument and a capillary apparatus. Samples for microanalysis were dried *in vacuo* to constant weight (20 °C, *ca.* 0.1 Torr) and analysed with a Fisons Instruments 1108 CHNS-O elemental analyser. UV-stability studies have been conducted with a Varian Caryl spectrometer. Electrical conductivity measurements (ΛM, reported as µS cm^2 mol^{-1}) of DMSO solutions of the complexes were recorded using a Crison CDTM 522 conductimeter at room temperature.

Single-crystal X-ray crystallography

The most relevant crystallographic data and structure refinement results for the compounds HL^2 and HL^4 and complexes **1** and **3** are given in Table S1.† Suitable crystals were selected and mounted on a XtaLAB Synergy R, DW system, HyPix-Arc 150 diffractometer, where intensities were collected at 140 K using Cu Kα radiation. The data sets were reduced and corrected for absorption using CrysAlis^{Pro}.[27] The structures were solved with the ShelXT solution program[28] using dual methods and by using Olex2 1.5 as the graphical interface.[29] All non-hydrogen atoms were refined anisotropically using full-matrix least-squares based on $|F|^2$. Hydrogen atoms were placed at calculated positions using the 'riding' model. The CCDC numbers 2424467, 2424469, 2424470 and 2424471† contain the crystallographic data for compounds HL^2 and HL^4 and complexes **1** and **3**, respectively. Another experimental X-ray determination of complex **3** was carried out, which has been deposited as CCDC 2424472, but was not discussed here because it has a higher R value.

Computational details

The electronic structure and geometries of the precursor ligands HL^1–HL^4, their L^1–L^4 anions, and complexes **1–4** were calculated using DFT at the B3LYP level[30,31] with the 6-311G* basis set and the LANL2DZ basis set[32] for the Ru atom. Molecular geometries of HL^2, HL^4, **1** and **3** were optimised by starting from the crystallographic coordinates. Frequency calculations were carried out at the same level of theory to identify all the stationary points as minima (zero imaginary frequencies). DFT calculations were performed with the Gaussian 09 suite of programs.[33] The theoretical IR spectra were scaled by a factor of 0.96.[34,35] The coordinates of all optimised compounds are reported in Table S7.†

Cell Culture and cytotoxicity tests

Cell lines were grown in a humidified 5% CO$_2$ environment at 37 °C in dedicated media. Specifically, growth media were MEM supplemented with 10% FBS, 1% sodium pyruvate, antibiotic, and antimycotic for MCF-7, Caco-2 and HepG2.

MCF-10A cells were cultured in a DMEM/F12 Ham's mixture supplemented with 5% equine serum, 20 ng mL^{-1} EGF, 10 µg mL^{-1} insulin, 0.5 mg mL^{-1} hydrocortisone, antibiotics, and antimycotics. The effect exerted on cell viability by the metal complexes was determined by 3-(4,5-dimethylthiazol-2-yl)-2,5-diphenyltetrazolium bromide (MTT) assay.[36] After individual 72 h treatments with 0–100 µM of the bd-curcuminoid ligands and the corresponding Ru-complexes, MTT was added to the culture media at a final concentration of 0.5 mg mL^{-1} and incubated for 2 h at 37 °C. Cisplatin was used as positive control. The medium was replaced with 100 µL of DMSO, and after 10 min the optical density was recorded at 550 nm on a microplate reader. All compounds were dissolved in DMSO, with its concentration maintained at 1% during cellular assays to minimize cytotoxic effects arising from the vehicle. Cells treated with 1% DMSO served as the control throughout the experiments. At least six replicates were performed for each data point. Chemicals (Merck-Sigma – Milan, Italy) and plasticwares (Corning – Milan, Italy) were cell culture grade.

Proliferation and apoptotic marker analysis

Western blotting assays were used to analyse the levels of proliferating cell nuclear antigen (PCNA) and p62. Caco-2 cells were treated for 24 h with subtoxic levels (2 µM) of HL^1 and complex **1**. Upon lysis, protein lysates were separated using 12% SDS-PAGE, then electroblotted onto PVDF membranes. The membranes were then blocked overnight at 4 °C in TBS buffer (10mM Tris–HCl and 0.5 M NaCl) supplemented with 5% bovine serum albumin. Following the blocking step, the membranes were incubated with the specific primary monoclonal antibody, followed by incubation with a specific peroxidase-conjugated secondary monoclonal antibody. Immunoblot detection was achieved using an ECL western blotting analysis system. Enhanced ChemiLuminescence Western Blotting analysis system (Amersham-Pharmacia-Biotech) was used for immunoblotting detections. β-Actin served as an internal control to ensure equal protein loading. Densitometric quantification of the immunoblots was performed using Fiji software.[37]

Binding to DNA

DNA binding affinities and kinetic parameters were determined using a biosensor platform as described elsewhere.[38] A carboxylate-functionalized sensor surface was first activated *via* EDC/NHS chemistry to immobilize streptavidin. Prior to DNA immobilization, residual reactive carboxylic sites were blocked with ethanolamine.[39] A 5′-biotinylated double-stranded DNA oligonucleotide (sequence: 5′-GGTGTGGGATGGGACCAACCTACGATTACA-3′) was successively coupled to the streptavidin-coated surface. Curcuminoid derivatives and their corresponding ruthenium complexes were individually tested over a concentration range of 0.5–50 µM in phosphate-buffered saline (PBS, pH 7.4). Binding events were monitored in real-time until equilibrium stabilization, followed by dissociation phases in pure PBS buffer.

Surface regeneration between analyte injections was achieved using 10 mM glycine–HCl (pH 2.5).

Raw data were analyzed using dual kinetic models:

$$R(t) = R_{eq}(1 - e^{-k_{obs}t}) \tag{1}$$

$$R(t) = R_1(1 - e^{-k_{obs,1}t}) + R_2(1 - e^{-k_{obs,2}t}) \tag{2}$$

and the validity of each model was assessed by a standard F-test procedure.

Effect on proteasome activity. The inhibitory effects of curcuminoid ligands and their metal complexes on 20S proteasome activity were evaluated using synthetic fluorogenic peptide substrates (Suc-Leu-Leu-Val-Tyr-AMC, Z-Leu-Ser-Thr-Arg-AMC and Z-Leu-Leu-Glu-AMC for chymotrypsin-like, trypsin-like, and caspase-like activity, respectively).

Reaction mixtures contained isolated 20S proteasome (1 μg), test compounds (0–100 μM), substrate (20 μM), and 50 mM Tris–HCl buffer (pH 8.0) in a final volume of 100 μL. After incubation at 37 °C for 60 min, proteasomal cleavage of AMC (7-amino-4-methylcoumarin) was quantified using a SpectraMax Gemini XPS fluorescence microplate reader (λ_{exc} = 365 nm, λ_{em} = 449 nm).

Binding and inhibition of HMGR activity. HMGR surface was prepared as reported elsewhere,[40] and essentially as described for streptavidin in the preparation of the dsDNA surface. Surface-blocked HMGR was tested for binding to the compounds of interest at different concentrations in the range 0.1–100 μM. The biosensor chamber was set at 37 °C throughout. Raw data were analyzed with mono- and bi-exponential models, the validity of each model to fit time courses being assessed by F-test procedure. Next, the inhibitory effect of the molecules of interest was established according to a chromatographic method described elsewhere.[41] The residual activity of human HMGR was assessed after pre-incubating isolated HMGR (0.4 μM) with increasing concentrations (0.1–100 μM) of each test molecule for 60 min. The enzymatic reaction was initiated by adding 1.55 mM HMG-CoA and 2.68 mM NADPH, followed by a 60 min incubation at 37 °C. The reaction mixture was then analyzed using a Phenomenex Luna C18 reverse-phase HPLC column at 26 ± 0.1 °C. The assay monitored both the consumption rates of HMG-CoA and NADPH and the production rates of mevalonate and NADP⁺. Residual activity values were calculated from raw data using a standard model for reversible competitive inhibition.[42]

Syntheses of the pro-ligands

The proligand **HL³** has been previously described in the literature,[43] and a similar synthetic procedure was employed to prepare the **HL¹**, **HL²**, and **HL⁴** proligands, which have not been previously reported. Proligands **HL¹–HL⁴** were synthesised by dissolving bisdemethoxycurcumin (0.97 mmol) in acetone (9 mL), followed by the addition of triethylamine (TEA, 2.92 mmol). After 15 minutes, the appropriate carbonyl chloride (2.92 mmol) was added at 0 °C under N₂ atmosphere. The reaction mixture was stirred at room temperature. Thin layer chromatography (7 : 3 hexane/ethylacetate) displayed the disappearance of bisdemethoxycurcumin and the formation of a faster running yellow spot after 4 hours. The resulting yellow precipitate was filtered with acetone and then purified by crystallization with dichloromethane/ethanol giving the final proligand as yellow powder.

HL¹. To a solution of bisdemethoxycurcumin (300 mg, 0.97 mmol) in acetone (9 mL), was mixed triethylamine (TEA 0.41 mL, 2.92 mmol) and then cyclopentanecarbonyl chloride (0.35 mL, 2.92 mmol) was added. The proligand **HL¹** (369 mg, yield 76%), is soluble in DMSO and chlorinated solvents, slightly soluble in alcohols, acetone and CH₃CN, and insoluble in H₂O and n-hexane. Anal. Calcd for $C_{31}H_{32}O_6$: C, 74.38; H, 6.44. Found: C, 74.44; H, 6.41. m.p.: 219–220 °C. IR (cm⁻¹): 2950 m, 2870 m ν(aliphatic C–H); 1743 s ν(–OC=O), 1632 m ν(C=O); 1567 m, 1505 m, 1447 m ν(C=C); 1415 m, 1363 m, 1305 m, 1209 s, 1164 s, 1127 s, 1013 m, 967 s, 882 s, 860 s, 726 m, 696 m, 608 m. ¹H NMR (CDCl₃, 293 K): δ 1.69 m, 1.81 m [8H, C(12–12′)H], 1.99 m, 2.05 m [8H, C(11–11′)H], 3.02 [quint, 2H, C(10–10′)H], 5.86 [s, 1H, C(1)H], 6.60 [d, 2H, C(3–3′)H, ^3J = 16 Hz], 7.15 [d, 4H, C(7–7′)H, ^3J = 9 Hz], 7.59 [d, 4H, C(6–6′)H, ^3J = 9 Hz], 7.67 [d, 2H, C(4–4′)H, ^3J = 16 Hz], ¹³C{¹H} NMR (CDCl₃, 293 K): δ 25.9 [C(12–12′)], 30.1 [C(11–11′)], 43.9 [C(10–10′)], 101.9 [C(1)], 122.2 [C(7–7′)], 124.1 [C(3–3′)], 129.2 [C(6–6′)], 132.5 [C(5–5′)], 139.6 [C(4–4′)], 152.3 [C(8–8′)], 175.0 [C(9–9′)], 183.2 [C(2–2′)=O]. ESI-MS(−) CH₃OH (m/z [relative intensity, %]): 499 [100] [L¹]⁻.

HL². To a solution of bisdemethoxycurcumin (300 mg, 0.97 mmol) in acetone (9 mL), was mixed triethylamine (TEA 0.41 mL, 2.92 mmol) and then heptanoyl chloride (0.45 mL, 2.92 mmol) was added. The proligand **HL²** (252 mg, yield 49%) is soluble in DMSO and chlorinated solvents, slightly soluble in alcohols, acetone and CH₃CN, and insoluble in H₂O and n-hexane. Anal. Calcd for $C_{33}H_{40}O_6$: C, 74.41; H, 7.57. Found: C, 74.35; H, 7.59. m.p.: 171–172 °C. IR (cm⁻¹): 2957 w, 2927 s, 2853 w ν(aliphatic C–H); 1756 s ν(–OC=O), 1627 m ν(C=O); 1586 m, 1556 m, 1506 m, 1465 m, 1414 m ν(C=C); 1379 m, 1344 w, 1320 w, 1283 w, 1213 s, 1165 s, 1133 s, 1105 s, 1036 m, 1014 m, 977 s, 955 s, 922 s, 865 m, 842 vs, 796 m, 779 m, 723 s. ¹H NMR (CDCl₃, 293 K): δ 0.94 [t, 6H, C(15–15′)H], 1.37 [m, 8H, C(14–14′)H and C(13–13′)H], 1.45 [m, 4H, C(12–12′)H], 1.78 [quint, 4H, C(11–11′)H], 2.59 [t, 4H, C(10–10′)H], 5.86 [s, 1H, C(1)H], 6.60 [d, 2H, C(3–3′)H, ^3J = 16 Hz], 7.15 [d, 4H, C(7–7′)H, ^3J = 9 Hz], 7.59 [d, 4H, C(6–6′)H, ^3J = 9 Hz], 7.67 [d, 2H, C(4–4′)H, ^3J = 16 Hz]. ¹³C{¹H} NMR (CDCl₃, 293 K): δ 13.9 [C(15–15′)], 22.4 [C(14–14′)], 24.8 [C(11–11′)], 28.7 [C(12–12′)], 31.4 [C(13–13′)], 34.4 [C(10–10′)], 101.8 [C(1)], 122.1 [C(7–7′)], 124.1 [C(3–3′)], 129.2 [C(6–6′)], 132.6 [C(5–5′)], 139.5 [C(4–4′)], 152.1 [C(8–8′)], 172.1 [C(9–9′)], 182.7 [C(2–2′)=O]. ESI-MS(−) CH₃OH (m/z [relative intensity, %]): 531 [100] [L²]⁻.

HL³. To a solution of bisdemethoxycurcumin (300 mg, 0.97 mmol) in acetone (9 mL), was mixed triethylamine (TEA 0.27 mL, 1.95 mmol) and then furan-2-carbonyl chloride (0.29 mL, 2.92 mmol) was added. The proligand **HL³** (218 mg, yield 45%) is soluble in DMSO and chlorinated solvents, slightly soluble in alcohols, acetone and CH₃CN, and insoluble in H₂O and n-hexane. Anal. Calcd for $C_{29}H_{20}O_8$: C,70.16; H,

4.06. Found: C,70.04; H, 4.14; m.p.: 211–212 °C. IR (cm^{-1}): 3140 w, 3113 w ν(aromatic C–H); 1747 m, 1732 s ν(–OC=O), 1628 m, 1601 m ν(C=O); 1586 m, 1565 m, 1506 s, 1465 s, 1418 m ν(C=C); 1393 s, 1321 m, 1296 s, 1234 m, 1213 s, 1172 s, 1133 s, 1070 vs, 1013 s, 964 s, 932 s, 884 s, 847 s, 793 s, 781 s, 747 s, 727 s, 693 m, 651 m. ^{1}H NMR (DMSO, 293 K): δ 6.21 [s, 1H, C(1)H], 6.82 [dd, 2H, C(12–12′)H], 6.99 [d, 2H, C(3–3′)H, ^3J = 16 Hz], 7.38 [d, 4H, C(7–7′)H, ^3J = 9 Hz], 7.60 [d, 2H, C(11–11′)H], 7.70 [d, 2H, C(4–4′)H, ^3J = 16 Hz], 7.85 [d, 4H, C(6–6′)H, ^3J = 9 Hz], 8.12 [d, 2H, C(13–13′)H]. ^{13}C{^{1}H} NMR (DMSO, 293K): δ 102.4 [C(1)], 113.3 [C(12–12′)], 120.9 [C(11–11′)], 123.0 [C(7–7′)], 125.1 [C(3–3′)], 130.2 [C(6–6′)], 133.2 [C(5–5′)], 139.8 [C(4–4′)], 143.3 [C(10–10′)], 149.3 [C(13–13′)], 151.7 [C(8–8′)], 156.6 [C(9–9′)], 183.6 [C(2–2′)=O]. ESI-MS(−) CH$_3$OH (m/z [relative intensity, %]): 495 [100] [L^3]$^-$.

HL^4. To a solution of bisdemethoxycurcumin (300 mg, 0.97 mmol) in acetone (9 mL), was mixed triethylamine (TEA 0.41 mL, 2.92 mmol) and then 3,3-dimethylbutyryl chloride (0.41 mL, 2.92 mmol) was added. The proligand **HL^4** (247 mg, yield 50%) is soluble in DMSO and chlorinated solvents, slightly soluble in alcohols, acetone and CH$_3$CN, and insoluble in H$_2$O and n-hexane. Anal. Calcd for C$_{31}$H$_{36}$O$_6$: C, 73.79; H, 7.19. Found: C, 73.89; H, 7.21. m.p.: 203–204 °C. IR (cm^{-1}): 2959 w, 2904 w, 2868 w ν(aliphatic C–H); 1754 s ν(–OC=O), 1626 m ν(C=O); 1595 m, 1580 m, 1535 m, 1506 s, 1469 m, 1415 m ν(C=C); 1365 m, 1350 m, 1314 m, 1207 s, 1188 s, 1164 s, 1140 m, 1106 s, 1014 m, 975 s, 956 s, 927 s, 898 s, 838 s, 800 m, 785 m, 727 m, 615 m. ^{1}H NMR (CDCl$_3$, 293 K): δ 1.17 [s, 18H, C(12–12′)H], 2.47 [s, 4H, C(10–10′)H], 5.86 [s, 1H, C(1)H], 6.60 [d, 2H, C(3–3′)H, ^3J = 16 Hz], 7.15 [d, 4H, C(7–7′)H, ^3J = 9 Hz], 7.59 [d, 4H, C(6–6′)H, ^3J = 9 Hz], 7.67 [d 2H, C(4–4′)H, ^3J = 16 Hz]. ^{13}C{^{1}H} NMR (CDCl$_3$, 293 K): δ 29.7 [C(12–12′)], 31.2 [C(11–11′)], 47.8 [C(10–10′)], 101.8 [C(1)], 122.3 [C(7–7′)], 124.1 [C(3–3′)], 129.2 [C(6–6′)], 132.6 [C(5–5′)], 139.6 [C(4–4′)], 152.0 [C(8–8′)], 170.4 [C(9–9′)], 183.2 [C(2–2′)=O]. ESI-MS(−) CH$_3$OH (m/z [relative intensity, %]): 503 [100] [L^4]$^-$.

[Ru(p-cym)(L^1)Cl] (1). The proligand **HL^1** (200 mg, 0.4 mmol) and triethylamine (TEA 56 μL, 0.4 mmol) were dissolved in CH$_3$CN (5 mL) at 50 °C. After 30 minutes, [(p-cymene)RuCl$_2$]$_2$ (122 mg, 0.2 mmol) was added. The resulting red solution was stirred under reflux for 16 hours. The solvent was then dried under reduced pressure and the residue was dissolved with CH$_2$Cl$_2$ and precipitated with hexane. The red precipitate was filtered and washed with cold 2-propanol to ensure the removal of the triethylammonium chloride formed during the reaction. **1** (152 mg, 50% yield) is soluble in DMSO, CH$_3$CN and chlorinated solvents, slightly soluble in alcohols and insoluble in H$_2$O. Anal. Calcd for C$_{41}$H$_{45}$ClO$_6$Ru: C, 63.93, H, 5.89 Found: C, 63.84; H, 5.82, m.p.: 202–203 °C. IR (cm^{-1}): 2957 w, 2868 w ν(aliphatic C–H); 1748 s ν(–OC=O), 1630 m ν(C=O); 1598 m, 1517 s, 1506 s, 1455 m, 1405 m ν(C=C); 1365 m, 1308 m, 1284 m, 1212 m, 1163 s, 1123 s, 1033 m, 1015 m, 991 m, 969 s, 884 m, 862 m, 803 m, 738 m, 684 m, 645 m, 281 s ν(Ru–Cl). ^{1}H NMR (CDCl$_3$, 293 K): δ 1.42 [d, 6H, –CH(CH_3)$_2$ of p-cym, ^4J = 7Hz], 1.69 m, 1.81 m [8H, C(12–12′)H], 1.99 m, 2.05 m [8H, C(11–11′)H], 2.37 [s, 3H, –CH_3 of

p-cym], 3.02 quint, 3.02 sept [3H, C(10–10′)H of ligand and –CH(CH$_3$)$_2$ of p-cym], 5.33 d, 5.60 d [4H, aa′bb′ system, CH$_3$–C$_6$H$_4$–CH(CH$_3$)$_2$ of p-cym, ^3J = 6 Hz], 5.49 [s, 1H, C(1)H], 6.54 [d, 2H, C(3–3′)H, ^3J = 16 Hz], 7.11 [d, 4H, C(7–7′)H, ^3J = 9 Hz], 7.53 [d, 4H, C(6–6′)H, ^3J = 9 Hz], 7.60 [d, 2H, C(4–4′)H, ^3J = 16 Hz]. ^{13}C{^{1}H} NMR (CDCl$_3$, 293 K): δ 18.0 [–CH$_3$ of p-cym], 22.4 [–CH(CH$_3$)$_2$ of p-cym], 25.9 [C(12–12′)], 30.1 [C(11–11′)], 30.9 [–CH(CH$_3$)$_2$ of p-cym], 43.9 [C(10–10′)], 79.2 [C(a–a′) of p-cym], 83.0 [C(b–b′) of p-cym], 97.5 [Ci′ of p-cym], 99.7 [Ci of p-cym], 102.4 [C(1)], 121.9 [C(7–7′)], 127.7 [C(3–3′)], 128.7 [C(6–6′)], 133.4 [C(5–5′)], 137.8 [C(4–4′)], 151.7 [C(8–8′)], 175.0 [C(9–9′)], 178.4 [C(2–2′)=O]. ESI-MS(+) CH$_3$CN (m/z [relative intensity, %]): 735 [100] [Ru(p-cym)(L^1)]$^+$. Λ_m (T = 298K, DMSO, 10^{-5} mol L^{-1}): 10 (t = 0), 10 (t = 24h), 11 (t = 48h), 11 (t = 72h) μS cm^2 mol^{-1}.

[(p-cym)Ru(L^2)Cl] (2). The complex has been synthesised following the same procedure as reported for **1** by using **HL^2** as proligand. **2** (187 mg, yield 57%) is soluble in DMSO, CH$_3$CN and chlorinated solvents, slightly soluble in alcohols and insoluble in H$_2$O. Anal. Calcd for C$_{43}$H$_{53}$ClO$_6$Ru: C, 64.37, H, 6.66. Found: C, 64.40; H, 6.53. m.p.: 152–153 °C. IR (cm^{-1}): 3064 w, 3033 w, 2926 w, 2871 w, 2857 w ν(aliphatic C–H); 1759 m ν(–OC=O), 1635 m ν(C=O); 1600 w, 1582 w, 1532 s, 1505 s, 1467 m, 1427 m, 1409 m ν(C=C); 1387 m, 1375 m, 1341 w, 1322 w, 1290 w, 1265 w, 1210 m, 1164 s, 1142 s, 1129 s, 1101 vs, 1014 m, 975 m, 944 m, 919 m, 907 m, 866 m, 834 m, 820 m, 806 m, 727 m, 690 w, 278 s ν(Ru–Cl). ^{1}H NMR (CDCl$_3$, 293 K): δ 0.94 [t, 6H, C(15–15′)H], 1.37 [m, 8H, C(13–13′)H and C(14,14′)H], 1.42 [d, 6H, –CH(CH_3)$_2$ of p-cym, ^4J = 7Hz], 1.45 [m, 4H, C(12–12′)H], 1.78 [quint., 4H, C(11–11′)H], 2.36 [s, 3H, –CH_3 of p-cym], 2.59 [t, 4H, C(10–10′)H], 3.01 [sept, 1H, –CH(CH$_3$)$_2$ of p-cym], 5.33 d, 5.60 d [4H, aa′bb′ system, CH$_3$–C$_6$H$_4$–CH(CH$_3$)$_2$ of p-cym, ^3J = 6 Hz], 5.49 [s, 1H, C(1)H], 6.54 [d, 2H, C(3–3′)H, ^3J = 16 Hz], 7.11 [d, 4H, C(7–7′)H, ^3J = 9 Hz], 7.53 [d, 4H, C(6–6′)H, ^3J = 9 Hz], 7.60 [d, 2H, C(4–4′)H, ^3J = 16 Hz]. ^{13}C{^{1}H} NMR (CDCl$_3$, 293 K): δ 14.0 [C(15–15′)], 18.0 [–CH$_3$ of p-cym], 22.4 [–CH(CH$_3$)$_2$ of p-cym], 22.5 [C(14–14′)], 24.9 [C(11–11′)], 28.8 [C(12–12′)], 30.9 [–CH(CH$_3$)$_2$ of p-cym], 31.4 [C(13–13′)], 34.4 [s, C(10–10′)], 79.2 [C(a–a′) of p-cym], 83.0 [C(b–b′) of p-cym], 97.6 [Ci′ of p-cym], 99.7 [Ci of p-cym], 102.5 [C(1)], 122.0 [C(7–7′)], 127.7 [C(3–3′)], 128.8 [C(6–6′)], 133.5 [C(5–5′)], 137.7 [C(4–4′)], 151.5 [C(8–8′)], 172.1 [C(9–9′)], 178.4 [C(2–2′)=O]. ESI-MS(+) CH$_3$CN (m/z [relative intensity, %]): 767 [100] [Ru(p-cym)(L^2)]$^+$. Λ_m (T = 298K, DMSO, 10^{-5} mol L^{-1}): 10 (t = 0), 10 (t = 24h), 10 (t = 48h), 10 (t = 72h) μS cm^2 mol^{-1}.

[(p-cym)Ru(L^3)Cl] (3). The complex has been synthesised following the same procedure as reported for **1** by using **HL^3** as proligand. After 16 hours of reflux, the precipitate was filtered giving the final complex as a red powder (226 mg, yield 74%). **3** is soluble in DMSO and chlorinated solvents, slightly soluble in CH$_3$CN and alcohols and insoluble in H$_2$O. Anal. Calcd for C$_{39}$H$_{33}$ClO$_8$Ru: C, 61.14, H, 4.34. Found: C, 61.21, H, 4.41. m.p.: 267–268 °C. IR (cm^{-1}): 3141 w, 3128 w, 3112 w, 3037 w, 2923 w, 2866 w ν(aromatic C–H); 1732 m ν(–OC=O), 1627 m ν(C=O); 1599 w, 1568 w, 1541 m, 1509 s, 1467 s, 1401 s

ν(C=C); 1330 w, 1319 w, 1295 s, 1231 m, 1204 s, 1172 s, 1159 s, 1090 s, 1010 m, 998 m, 990 m, 977 m, 969 m, 948 m, 928 m, 883 m, 869 m, 853 m, 825 m, 805 m, 796 m, 768 m, 751 m, 734 m, 685 m, 610 m, 276 s ν(Ru–Cl). ^{1}H NMR (CDCl$_3$, 293 K): δ 1.43 [d, 6H, –CH(CH$_3$)$_2$ of p-cym, ^4J = 7Hz], 2.38 [s, 3H, –CH$_3$ of p-cym], 3.02 [sept, 1H, –CH(CH$_3$)$_2$ of p-cym], 5.34 d, 5.61 d [4H, aa′bb′ system, CH$_3$–C$_6$H$_4$–CH(CH$_3$)$_2$ of p-cym, ^3J = 6 Hz], 5.51 [s, 1H, C(1)H], 6.58 [d, 2H, C(3–3′)H, ^3J = 16 Hz], 6.63 [m, 2H, C(12–12′)H], 7.26 [d, 4H, C(7–7′)H, ^3J = 9 Hz], 7.42 [d, 2H, C(11–11′)H], 7.59 [d, 4H, C(6–6′)H, ^3J = 9 Hz], 7.63 [d, 2H, C(4–4′)H, ^3J = 16 Hz], 7.72 [s, 2H, C(13–13′)H]. ^{13}C{^{1}H} NMR (CDCl$_3$, 293 K): δ 18.0 [–CH$_3$ of p-cym], 22.4 [–CH(CH$_3$)$_2$ of p-cym], 30.9 [–CH(CH$_3$)$_2$ of p-cym], 79.2 [C(a–a′) of p-cym], 83.1 [C(b–b′) of p-cym], 97.6 [Ci′ of p-cym], 99.7 [Ci of p-cym], 102.6 [C(1)], 112.3 [C(12–12′)], 119.7 [C(11–11′)], 122.0 [C(7–7′)], 127.9 [C(3–3′)], 128.9 [C(6–6′)], 133.8 [C(5–5′)], 137.7 [C(4–4′)], 143.9 [C(10–10′)], 147.3 [C(13–13′)], 150.9 [C(8–8′)], 156.2 [C(9–9′)], 178.4 [C(2–2′)=O]. ESI-MS(+) CH$_3$CN (m/z [relative intensity, %]): 731 [100] [Ru(p-cym)(L^3)]$^+$. Λ_m (T = 298K, DMSO, 10^{-5} mol L^{-1}): 10 (t = 0), 11 (t = 24h), 11 (t = 48h), 12 (t = 72h) μS cm^2 mol^{-1}.

[Ru(p-cym)(L^4)Cl] (4). The complex has been synthesised following the same procedure as reported for (1) by using **HL^4** as proligand. **4** (183 mg, yield 59%) is soluble in DMSO, CH$_3$CN and chlorinated solvents, slightly soluble in alcohols and insoluble in H$_2$O. Anal. Calcd for C$_{41}$H$_{49}$ClO$_6$Ru: C, 63.59, H, 6.38. Found: C, 63.72, H, 6.50. m.p.: 227–228 °C. IR (cm^{-1}): 2961 w, 2930 w, 2871 w ν(aliphatic C–H); 1751 m ν(–OC=O), 1635 m ν(C=O); 1598 w, 1586 w, 1533 s, 1506 m, 1472 m, 1408 m ν(C=C); 1368 m, 1321 m, 1281 w, 1210 m, 1186 s, 1163 s, 1110 s, 1033 m, 1013 m, 976 m, 926 m, 896 m, 875 m, 842 m, 806 w, 723 w, 714 w, 620 m, 280 s ν(Ru–Cl). ^{1}H NMR (CDCl$_3$, 293 K): δ 1.16 [s, 18H, C(12–12′)H], 1.42 [d, 6H, –CH(CH$_3$)$_2$ of p-cym, ^4J = 7 Hz], 2.36 [s, 3H, –CH$_3$ of p-cym], 2.47 [s, 4H, C(10–10′)H], 3.01 [sept, 1H, –CH(CH$_3$)$_2$ of p-cym], 5.33 d, 5.60 d [4H, aa′bb′ system, CH$_3$–C$_6$H$_4$–CH(CH$_3$)$_2$ of p-cym, ^3J = 6 Hz], 5.50 [s, 1H, C(1)H], 6.54 [d, 2H, C(3–3′)H, ^3J = 16 Hz], 7.11 [d, 4H, C(7–7′)H, ^3J = 9 Hz], 7.53 [d, 4H, C(6–6′)H, ^3J = 9 Hz], 7.60 [d, 2H, C(4–4′)H, ^3J = 16 Hz]. ^{13}C{^{1}H} NMR (CDCl$_3$, 293 K): δ 18.0 [–CH$_3$ of p-cym], 22.4 [–CH(CH$_3$)$_2$ of p-cym], 29.7 [C(12–12′)], 30.9 [–CH(CH$_3$)$_2$ of p-cym], 31.2 [C(11–11′)], 47.9 [C(10–10′)], 79.2 [C(a–a′) of p-cym], 83.0 [C(b–b′) of p-cym], 97.6 [Ci′ of p-cym], 99.7 [Ci of p-cym], 102.4 [C(1)], 122.0 [C(7–7′)], 127.7 [C(3–3′)], 128.8 [C(6–6′)], 133.5 [C(5–5′)], 137.7 [C(4–4′)], 151.4 [C(8–8′)], 170.5 [C(9–9′)], 178.4 [C(2–2′)=O]. ESI-MS(+) CH$_3$CN (m/z [relative intensity, %]): 739 [100] [Ru(p-cym)(L^4)]$^+$. Λm (T = 298 K, DMSO, 10^{-5} mol L^{-1}): 9 (t = 0), 10 (t = 24h), 10 (t = 48h), 11 (t = 72h) μS cm^2 mol^{-1}.

Author contributions

The manuscript was written through contributions of all authors. All authors have given approval to the final version of the manuscript. The authors declare no competing financial interest.

Conflicts of interest

There are no conflicts to declare.

Data availability

The data supporting this article have been included as part of the ESI.†

It contains all the crystallographic details; the DFT calculations; monodimensional ^{1}H and ^{13}C NMR spectra and bidimensional {^{1}H–^{1}H}-COSY, {^{1}H–^{13}C}-HSQC, {^{1}H–^{13}C}-HMBC NMR spectra.

Acknowledgements

References

1 S. Abdolmaleki, A. Aliabadi and S. Khaksar, Riding the Metal Wave: A Review of the Latest Developments in Metal-Based Anticancer Agents, *Coord. Chem. Rev.*, 2024, **501**, 215579.

2 S. Alassadi, M. J. Pisani and N. J. Wheate, A Chemical Perspective on the Clinical Use of Platinum-Based Anticancer Drugs, *Dalton Trans.*, 2022, **51**(29), 10835–10846.

3 D. Karati, S. Meur, S. Mukherjee and S. Roy, Revolutionizing Anticancer Treatment: Ruthenium-Based Nanoplatforms Pave New Paths, *Coord. Chem. Rev.*, 2024, **519**, 216118.

4 M. Bashir, I. A. Mantoo, F. Arjmand, S. Tabassum and I. Yousuf, An Overview of Advancement of Organoruthenium(ii) Complexes as Prospective Anticancer Agents, *Coord. Chem. Rev.*, 2023, **487**, 215169.

5 S. Y. Lee, C. Y. Kim and T.-G. Nam, Ruthenium Complexes as Anticancer Agents: A Brief History and Perspectives, *Drug Des., Dev. Ther.*, 2020, 5375–5392.

6 M. Cozmin, I. I. Lungu, C. Gutu, A. Stefanache, L. D. Duceac, B. D. Șoltuzu, D. Damir, G. Calin, E. R. Bogdan Goroftei, C. Grierosu and M. Boev, Turmeric: From Spice to Cure. A Review of the Anti-Cancer,

Radioprotective and Anti-Inflammatory Effects of Turmeric Sourced Compounds, *Front. Nutr.*, 2024, **11**, 1399888.

7 A. B. Kunnumakkara, M. Hegde, D. Parama, S. Girisa, A. Kumar, U. D. Daimary, P. Garodia, S. C. Yenisetti, O. V. Oommen and B. B. Aggarwal, Role of Turmeric and Curcumin in Prevention and Treatment of Chronic Diseases: Lessons Learned from Clinical Trials, *ACS Pharmacol. Transl. Sci.*, 2023, **6**(4), 447–518.

8 T. Esatbeyoglu, P. Huebbe, I. M. A. Ernst, D. Chin, A. E. Wagner and G. Rimbach, Curcumin—From Molecule to Biological Function Angewandte, *Angew. Chem., Int. Ed.*, 2012, **51**, 5308–5332.

9 M. H. Shahrajabian and W. Sun, The Golden Spice for Life: Turmeric with the Pharmacological Benefits of Curcuminoids Components, Including Curcumin, Bisdemethoxycurcumin, and Demethoxycurcumins, *Curr. Org. Synth.*, 2024, **21**(5), 665–683.

10 K. M. Nelson, J. L. Dahlin, J. Bisson, J. Graham, G. F. Pauli and M. A. Walters, The Essential Medicinal Chemistry of Curcumin, *J. Med. Chem.*, 2017, **60**(5), 1620–1637.

11 S. Beganovic and C. Wittmann, Medical Properties, Market Potential, and, Microbial Production of Golden Polyketide Curcumin for Food, Biomedical, and Cosmetic Applications, *Curr. Opin. Biotechnol.*, 2024, **87**, 103112.

12 G. Jin, W. Xu, H. Tang, Y. Cui and H. Zhang, Bisdemethoxycurcumin, a Curcumin, Protects Chondrocytes, and Reduces Cartilage Inflammation via the NRF2/HO-1/NLRP3 Pathway, *Immun., Inflammation Dis.*, 2024, **12**(2), e1195.

13 T. Abdul-Rahman, W. A. Awuah, T. Mikhailova, J. Kalmanovich, A. Mehta, J. C. Ng, M. A. Coghlan, M. Zivcevska, A. J. Tedeschi, E. C. de Oliveira, A. Kumar, E. Cantu-Herrera, M. Lyndin, K. Sikora, A. Alexiou, A. L. Bilgrami, K. M. Al-Ghamdi, A. Perveen, M. Papadakis and G. M. Ashraf, Antioxidant, Anti-Inflammatory and Epigenetic Potential of Curcumin in Alzheimer's Disease, *BioFactors*, 2024, **50**(4), 693–708.

14 Y. Xiang, B. Fan, P. Shang, R. Ding, J. Du, T. Zhu, H. Zhang and X. Yan, VR23 and Bisdemethoxycurcumin Enhanced Nanofiber Niche with Durable Bidirectional Functions for Promoting Wound Repair and Inhibiting Scar Formation, *Small Methods*, 2024, **8**(12), 2400273.

15 Y. Song, J. Ruan, S. Liu and H. Yu, Bisdemethoxycurcumin Augments Docetaxel Efficacy for Treatment of Prostate Cancer, *Biol. Pharm. Bull.*, 2024, **47**(8), 1437–1446.

16 P. Srivastava, M. Shukla, G. Kaul, S. Chopra and A. K. Patra, Rationally Designed Curcumin Based Ruthenium(II) Antimicrobials Effective against Drug-Resistant Staphylococcus Aureus, *Dalton Trans.*, 2019, **48**(31), 11822–11828.

17 S. Li, G. Xu, Y. Zhu, J. Zhao and S. Gou, Bifunctional Ruthenium(II) Polypyridyl Complexes of Curcumin as Potential Anticancer Agents, *Dalton Trans.*, 2020, **49**(27), 9454–9463.

18 R. Pettinari, F. Marchetti, F. Condello, C. Pettinari, G. Lupidi, R. Scopelliti, S. Mukhopadhyay, T. Riedel and P. J. Dyson, Ruthenium(II)-Arene RAPTA Type Complexes Containing Curcumin and Bisdemethoxycurcumin Display Potent and Selective Anticancer Activity, *Organometallics*, 2014, **33**(14), 3709–3715.

19 N. Pagliaricci, R. Pettinari, F. Marchetti, A. Tombesi, S. Pagliaricci, M. Cuccioloni, A. Galindo, F. Fadaei-Tirani, M. Hadiji and P. J. Dyson, Ru(II)-Arene Complexes of Curcumin and Bisdesmethoxycurcumin Metabolites, *Inorg. Chem.*, 2024, **63**(17), 7955–7965.

20 R. Pettinari, A. Petrini, F. Marchetti and D. Nicola, Influence of Functionalized H6-Arene Rings on Ruthenium (II) Curcuminoids Complexes, *ChemistrySelect*, 2018, **3**, 6696–6700.

21 M. Cuccioloni, L. Bonfili, M. Mozzicafreddo, V. Cecarini, R. Pettinari, F. Condello, C. Pettinari, F. Marchetti, M. Angeletti and A. M. Eleuteri, A Ruthenium Derivative of Quercetin with Enhanced Cholesterol-Lowering Activity, *RSC Adv.*, 2016, **6**(46), 39636–39641.

22 M. Cuccioloni, L. Bonfili, V. Cecarini, M. Nabissi, R. Pettinari, F. Marchetti, R. Petrelli, L. Cappellacci, M. Angeletti and A. M. Eleuteri, Exploring the Molecular Mechanisms Underlying the in Vitro Anticancer Effects of Multitarget-Directed Hydrazone Ruthenium(II)-Arene Complexes, *ChemMedChem*, 2020, **15**(1), 105–113.

23 J. Moscat and M. T. Diaz-Meco, P62 at the Crossroads of Autophagy, Apoptosis, and Cancer, *Cell*, 2009, **137**(6), 1001–1004.

24 W. Ma, S. Wei, Q. Li, J. Zeng, W. Xiao, C. Zhou, K. Y. Yoneda, A. A. Zeki and T. Li, Simvastatin Overcomes Resistance to Tyrosine Kinase Inhibitors in Patient-Derived, Oncogene-Driven Lung Adenocarcinoma Models, *Mol. Cancer Ther.*, 2024, **23**(5), 700–710.

25 W. J. Liu, L. Ye, W. F. Huang, L. J. Guo, Z. G. Xu, H. L. Wu, C. Yang and H. F. Liu, P62 Links the Autophagy Pathway and the Ubiqutin-Proteasome System upon Ubiquitinated Protein Degradation, *Cell. Mol. Biol. Lett.*, 2016, **21**(1), 1–14.

26 M. S. Wilson and P. F. Schofield, Markers to Study Human Colonic Cell Proliferation, *Gut*, 1995, **36**(1), 152.

27 O. D. Rigaku, *CrysAlisPro Software System*, 2022.

28 G. M. Sheldrick, Foundations and Advances SHELXT-Integrated Space-Group and Crystal-Structure Determination, *Acta Crystallogr.*, 2015, 3–8.

29 O. V. Dolomanov, L. J. Bourhis, R. J. Gildea, J. A. K. Howard and H. Puschmann, Olex2: A Complete Structure Solution, Refinement and Analysis Program, *J. Appl. Crystallogr.*, 2009, **42**, 339–341.

30 A. D. Becke, Density–functional Thermochemistry. I. The Effect of the Exchange–only Gradient Correction, *J. Chem. Phys.*, 1992, **96**(3), 2155–2160.

31 C. Lee, W. Yang and R. G. Parr, Development of the Colle-Salvetti Correlation-Energy Formula into a Functional of the Electron Density, *Phys. Rev. B: Condens. Matter Mater. Phys.*, 1988, **37**(2), 785–789.

32 P. J. Hay and W. R. Wadt, Ab Initio Effective Core Potentials for Molecular Calculations. Potentials for K to Au

Including the Outermost Core Orbitals, *J. Chem. Phys.*, 1985, **82**(1), 299–310.

33 M. J. Frisch, G. W. Trucks, H. B. Schlegel, G. E. Scuseria, M. A. Robb, J. R. Cheeseman, G. Scalmani, V. Barone, G. A. Petersson, H. Nakatsuji, X. Li, M. Caricato, A. Marenich, J. Bloino, B. G. Janesko, R. Gomperts, B. Mennucci and D. J. Hratchian, *Gaussian 09. Revision B.01*, Gaussian, Inc., Wallingford, CT, 2016.

34 M. W. Wong, Vibrational Frequency Prediction Using Density Functional Theory, *Chem. Phys. Lett.*, 1996, **256**(4–5), 391–399.

35 A. P. Scott and L. Radom, Harmonic Vibrational Frequencies: An Evaluation of Hartree-Fock, Møller-Plesset, Quadratic Configuration Interaction, Density Functional Theory, and Semiempirical Scale Factors, *J. Phys. Chem.*, 1996, **100**(41), 16502–16513.

36 J. van Meerloo, G. J. L. Kaspers and J. Cloos, Cell Sensitivity Assays: The MTT Assay, in *Cancer Cell Culture: Methods and Protocols*, ed. I. A. Cree, Humana Press, Totowa, NJ, 2011, pp. 237–245.

37 J. Schindelin, I. Arganda-Carreras, E. Frise, V. Kaynig, M. Longair, T. Pietzsch, S. Preibisch, C. Rueden, S. Saalfeld, B. Schmid, J.-Y. Tinevez, D. J. White, V. Hartenstein, K. Eliceiri, P. Tomancak and A. Cardona, Fiji: An Open-Source Platform for Biological-Image Analysis, *Nat. Methods*, 2012, **9**(7), 676–682.

38 M. Cuccioloni, L. Bonfili, V. Cecarini, M. Nabissi, R. Pettinari, F. Marchetti, R. Petrelli, L. Cappellacci, M. Angeletti and A. M. Eleuteri, Exploring the Molecular Mechanisms Underlying the in Vitro Anticancer Effects of Multitarget-Directed Hydrazone Ruthenium(ii)–Arene Complexes, *ChemMedChem*, 2020, **15**(1), 105–113.

39 R. J. Davies, P. R. Edwards, H. J. Watts, C. R. Lowe, P. E. Buckle, D. Yeung, T. M. Kinning and D. V. Pollard-Knight, The Resonant Mirror: A Versatile Tool for the Study of Biomolecular Interactions, in *Techniques in protein chemistry*, Elsevier, 1994, vol. 5, pp. 285–292.

40 M. Cuccioloni, M. Mozzicafreddo, M. Spina, C. N. Tran, M. Falconi, A. M. Eleuteri and M. Angeletti, Epigallocatechin-3-Gallate Potently Inhibits the in Vitro Activity of Hydroxy-3-Methyl-Glutaryl-CoA Reductase [S], *J. Lipid Res.*, 2011, **52**(5), 897–907.

41 M. Mozzicafreddo, M. Cuccioloni, A. M. Eleuteri and M. Angeletti, Rapid Reverse Phase-HPLC Assay of HMG-CoA Reductase Activity, *J. Lipid Res.*, 2010, **51**(8), 2460–2463.

42 M. Mozzicafreddo, M. Cuccioloni, A. M. Eleuteri, E. Fioretti and M. Angeletti, Flavonoids Inhibit the Amidolytic Activity of Human Thrombin, *Biochimie*, 2006, **88**(9), 1297–1306.

43 D. W. Lee, J. Park and S. S. Yoon, Synthesis and Biological Evaluation of Curcumin Analogs as Antiplatelet Inhibitor, *Bull. Korean Chem. Soc.*, 2014, **35**, 1537–1540.